Cerebral Cortex Communications, 2020, **1**, 1–15

doi: 10.1093/texcom/tgaa051
Original Article

ORIGINAL ARTICLE

Sharp Wave-Ripples in Human Amygdala and Their Coordination with Hippocampus during NREM Sleep

Roy Cox[1], Theodor Rüber[1,2,3], Bernhard P. Staresina[4] and Juergen Fell[1]

[1]Department of Epileptology, University of Bonn, Bonn 53127, Germany, [2]Department of Neurology, Epilepsy Center Frankfurt Rhine-Main, Goethe University Frankfurt, Frankfurt am Main 60590, Germany, [3]Center for Personalized Translational Epilepsy Research (CePTER), Goethe University Frankfurt, Frankfurt am Main 60590, Germany and [4]School of Psychology, University of Birmingham, Birmingham, B15 2TT, UK

Address correspondence to Roy Cox, Department of Epileptology, University of Bonn, Bonn 53127, Germany. Email: roycox.roycox@gmail.com.

Abstract

Cooperative interactions between the amygdala and hippocampus are widely regarded as critical for overnight emotional processing of waking experiences, but direct support from the human brain for such a dialog is absent. Using overnight intracranial recordings in 4 presurgical epilepsy patients (3 female), we discovered ripples within human amygdala during nonrapid eye movement (NREM) sleep, a brain state known to contribute to affective processing. Like hippocampal ripples, amygdala ripples are associated with sharp waves, linked to sleep spindles, and tend to co-occur with their hippocampal counterparts. Moreover, sharp waves and ripples are temporally linked across the 2 brain structures, with amygdala ripples occurring during hippocampal sharp waves and *vice versa*. Combined with further evidence of interregional sharp-wave and spindle synchronization, these findings offer a potential physiological substrate for the NREM-sleep-dependent consolidation and regulation of emotional experiences.

Key words: amygdala, hippocampus, NREM sleep, ripples, sharp waves

Introduction

Human sleep plays a pivotal role in emotional processing, including the consolidation of emotional memory traces, modulation of affective reactivity, and regulation of general emotional well-being (Payne et al. 2008; Sterpenich et al. 2009; Walker 2009; Payne and Kensinger 2010, 2018; Talamini et al. 2013; Tempesta et al. 2018). Although such processes have traditionally been viewed as primarily dependent on rapid eye movement (REM) sleep (Wagner et al. 2001; Nishida et al. 2009; Baran et al. 2012; Payne et al. 2012; Groch et al. 2013; Wiesner et al. 2015), accumulating evidence suggests a contributing role for nonrapid eye movement (NREM) sleep as well, potentially in conjunction with REM sleep (Hauner et al. 2013; Cairney et al. 2014, 2015; Cellini et al. 2016; Lehmann et al. 2016; Cox et al. 2018). Such sleep-dependent emotional processing has been hypothesized to rely on coordinated activity between the amygdala (AMY) and hippocampus (HPC), key neural structures in emotion and memory processing, respectively (Girardeau et al. 2017). Supporting this view, neuronal spiking activity in the AMY–HPC system related to an aversive task is replayed during subsequent NREM (but not REM) sleep in animals (Girardeau et al. 2017). In contrast, while human neuroimaging studies indicate enhanced AMY–HPC communication during emotional memory retrieval after sleep compared to

Received: 15 June 2020; **Revised:** 5 August 2020; **Accepted:** 7 August 2020

wake (Payne and Kensinger 2011), direct evidence for AMY–HPC communication during human sleep is surprisingly absent.

Ripples, ~80-Hz oscillations found in human HPC (Staresina et al. 2015) and various neocortical (NC) areas (Clemens et al. 2007; Axmacher et al. 2008; Zhang et al. 2018; Norman et al. 2019; Vaz et al. 2019) are of potential interest for such AMY–HPC interactions. Sharp wave-ripple complexes in HPC (SPW-ripples; ripples superimposed on ~3-Hz sharp waves), mediate widespread communication between HPC and NC during NREM sleep (Logothetis et al. 2012; Helfrich et al. 2019; Ngo et al. 2020). In animals, neuronal replay preferentially occurs during SPW-ripples (Wilson and McNaughton 1994) and suppressing SPW-ripples impairs memory consolidation (Girardeau et al. 2009). Importantly, the aforementioned joint AMY–HPC replay underlying emotional memory consolidation similarly coincides with HPC SPW-ripples (Girardeau et al. 2017), pointing to a key role for ripples in the AMY–HPC dialog. Of note, ripple-like activity has been described in animal AMY (Ponomarenko et al. 2003; Haufler and Pare 2014), raising the possibility of coordinated ripples between these brain structures, but ripples have never been described in human AMY.

Beside their close association with SPWs, HPC ripples are nested within HPC and NC ~13-Hz sleep spindles and ~1-Hz slow oscillations (SOs) (Staresina et al. 2015; Cox et al. 2019), enhancing HPC–NC information exchange and consolidation (Maingret et al. 2016; Latchoumane et al. 2017; Ngo et al. 2020). Whether these additional oscillatory rhythms have a role to play in AMY–HPC communication, either on their own or in conjunction with ripples, also remains unexplored.

Invasive sleep recordings from human AMY are rare and available studies typically employ a reference site outside AMY (Nir et al. 2011; Muñoz-Torres et al. 2018), resulting in ambiguity regarding the origin of reported activity. Here, we analyzed overnight invasive electroencephalography (EEG) from 4 clinically monitored epilepsy patients, each selected to have 2 electrode contacts unequivocally implanted in AMY and 2 in HPC, enabling bipolar recordings from both structures. We set out to examine whether 1) human AMY expresses NREM ripple activity similar to HPC, 2) ripples are coordinated across these brain structures, 3) ripples are associated with other electrophysiological phenomena (SPWs, spindles, SOs) within or across regions, and 4) AMY–HPC coordination exists for other spectral bands. Note that we did not assess behavioral indices of emotional processing. We report the existence of SPW-ripples in human AMY, and bidirectional AMY–HPC ripple, SPW, and spindle interactions during NREM sleep, offering a potential physiological basis for various forms of NREM-related emotional processing.

Materials and Methods

Participants

We analyzed archival electrophysiological overnight sleep data in a sample of 4 (3 female) patients suffering from pharmacoresistant epilepsy (age: 26.8 ± 4.3 years, range: 23–31). This sample overlaps with ones reported previously (Wagner et al. 2010; Staresina et al. 2015; Cox et al. 2019, 2020; Rings et al. 2019). Patients had been epileptic for 15.3 ± 4.6 years (range: 10–20) and were receiving anticonvulsive medication at the moment of recording (Supplementary Table 1). All patients gave informed consent, the study was conducted according to the Declaration of Helsinki, and was approved by the ethics committee of the Medical Faculty of the University of Bonn.

Data Acquisition

Continuous invasive electrophysiological monitoring was performed with a combination of depth and subdural strip/grid electrodes, while additional noninvasive polysomnography (see below) was obtained on a single night after patients had been monitored for at least 7 days. Depth electrodes (AD-Tech) containing 8–10 cylindrical platinum-iridium contacts (length: 1.6 mm; diameter: 1.3 mm; center-to-center intercontact distance: 4.5 mm) were stereotactically implanted bilaterally along the longitudinal HPC axis.

Pre- and postimplantation 3D T1-weighted magnetic resonance image (MRI) scans were used to determine electrode locations. Preoperative T1 (resolution = 0.8 × 0.8 × 0.8 mm^3, TR = 1660 ms, TE = 2.54 ms, flip angle = 9°) was acquired using a 3.0 Tesla Magnetom Trio (Siemens Healthineers, Erlangen, Germany) with a 32-channel-coil. Postoperative T1 (resolution = 1 × 1 × 1 mm^3, TR = 11.09 ms, TE = 5.02 ms, flip angle = 8°) was conducted using an Achieva 3.0 Tesla Tx system (Philips Healthcare, Best, The Netherlands). Preprocessing and analyses of T1 volumes was done using FMRIB's Software Library 5.0 (FSL) (Jenkinson et al. 2012). Brain extractions (Smith 2002) were performed and followed by a bias-field correction (Zhang et al. 2001). Postoperative volumes were linearly registered to the preoperative volumes. Anatomical labels of the electrodes were determined by an experienced physician (TR) based on these subject-specific co-registered T1 volumes.

For each patient, we selected 2 pairs of adjacent contacts from the same depth electrode (right: 3, left: 1) contralateral to the epileptogenic side. HPC pairs were located in gray matter ($n = 3$) or in the gray/white matter border ($n = 1$) of the posterior half of the HPC. AMY pairs contained one contact centrally within AMY and one in anterior AMY bordering the temporal pole. For all contact pairs, the more posterior contact was considered the active electrode and the more anterior one the reference. Distance between HPC and AMY channel pairs was 31.5 ± 3.7 mm (range: 27–36). Additional noninvasive signals were recorded from the scalp (Cz, C3, C4, Oz, A1, A2), the outer canthi of the eyes for electrooculography (EOG), and the chin for electromyography (EMG). Signals were sampled at 1 kHz (Stellate GmbH) with hardware high- and low-pass filters at 0.01 and 300 Hz, respectively, using an average-mastoid reference. Offline sleep scoring was done in 20-s epochs based on scalp EEG, EOG, and EMG signals in accordance with Rechtschaffen and Kales criteria (Rechtschaffen and Kales 1968). Stages S3 and S4 were combined into a single N3 stage following the more recent criteria of the American Academy of Sleep Medicine (Silber et al. 2007).

Preprocessing and Artifact Rejection

All data processing and analysis was performed in Matlab (the Mathworks), using custom routines and EEGLAB functionality (Delorme and Makeig 2004). Preprocessing and artifact rejection details are identical to our previous reports (Cox et al. 2019, 2020). Briefly, mastoid-referenced data were high-pass (0.3 Hz) and notch (50 Hz and harmonics up to 300 Hz) filtered, and channel-specific thresholds (z-score > 6) of signal gradient and high-frequency (>250 Hz) activity were applied to detect and exclude epileptogenic activity. Artifact-free data "trials" of at least 3 s were kept for subsequent processing, resulting in a

total of 90.4 ± 70.1 min (range: 42.3–194.3) of NREM sleep (N2: 80.4 ± 69.0, 37.9–183.3 min; N3: 10.0 ± 3.8, 4.4–12.6 min).

Spectral Analysis

For each NREM trial and channel, we estimated power spectral density using Welch's method (Welch 1967) with 3-s windows and 80% overlap (0.244 Hz resolution). Mean spectra were determined with a weighted average approach using trial durations as weights. Next, we removed the spectra's 1/f component to better emphasize narrowband spectral peaks (Wen and Liu 2016; Haller et al. 2018). To this end, we first interpolated the notch-filtered region (50, 100, 150, and 200 Hz, ±5 Hz) of each spectrum (Modified Akima cubic Hermite algorithm). Then, we fit each spectrum according to af^b using log–log least squares regression (Miller et al. 2009; Vijayan et al. 2017) and subtracted it from the observed spectrum. Fitting range was restricted to the 4–175 Hz range to avoid the often observed flattening of the spectrum below ~4 and the ~200-Hz notch-interpolated data, similar to approaches applied to wake EEG (Dave et al. 2018; Sheehan et al. 2018). Adjusted spectra were resampled to log space (Martin 2001) and smoothed 3 times with a moving average window of length 5, as shown in Figure 2A and B.

Time-Frequency Decomposition

Continuous data were decomposed with a family of complex Morlet wavelets. Each trial was extended with 5 s on either side to minimize edge artifacts. Wavelets were defined in terms of desired temporal resolution according to:

$$\text{Wavelet} = e^{i2\pi tf} * e^{-4\ln(2)t^2/h^2} \quad (1)$$

where i is the imaginary operator, t is time in seconds, f is frequency (50 logarithmically spaced frequencies between 0.5 and 200 Hz), ln is the natural logarithm, and h is temporal resolution (full-width at half-maximum; FWHM) in seconds (Cohen 2019). We set h to be logarithmically spaced between 3 s (at 0.5 Hz) and 0.025 s (at 200 Hz), resulting in FWHM spectral resolutions of 0.3 and 35 Hz, respectively. Trial padding was trimmed from the convolution result, which was subsequently downsampled by a factor 4 to reduce the amount of data. We normalized functional connectivity and PAC metrics using surrogate approaches (see below). To make surrogate distributions independent of variable numbers and durations of trials, we first concatenated the convolution result of all trials of a given sleep stage and then segmented them into 60-s fragments (discarding the final, incomplete segment).

Functional Connectivity

For every 60-s segment and frequency band, AMY–HPC functional connectivity was assessed using amplitude envelope correlations (AEC) (Bruns et al. 2000) and the phase locking value (PLV) (Lachaux et al. 1999) as a measure of phase synchrony. AEC was calculated as the Spearman correlation between the magnitudes of the convolution result. PLV operated on the phase angle differences according to:

$$PLV = \left| \frac{1}{n} \sum_{t=1}^{n} e^{i(\Delta\varphi(t))} \right| \quad (2)$$

where i is the imaginary operator, $\Delta\varphi$ indicates phase difference (in radians), and t is the sample. We further created normalized versions of these metrics using a surrogate approach. Surrogates were constructed by repeatedly ($n = 100$) time shifting the phase or amplitude time series of one channel by a random amount between 1 and 59 s, and recalculating AEC and PLV for each iteration. These distributions were then used to z-score raw AEC and PLV values, as used in Figure 2C and D, respectively.

Cross-Frequency Phase-Amplitude Coupling

For every 60-s segment, PAC was determined between all pairs of modulating frequency $f1$ and modulated frequency $f2$, where $f2 > 2{*}f1$. We employed an adaptation of the mean vector length method (Canolty et al. 2006) that adjusts for possible bias stemming from nonsinusoidal shapes of $f1$ (van Driel et al. 2015). Specifically, debiased phase-amplitude coupling strength (dPAC) was calculated as:

$$\text{dPAC} = \left| \frac{1}{n} \sum_{t=1}^{n} \left(\text{amp}_{f2}(t) * \left(e^{i\varphi_{f1}(t)} - B \right) \right) \right| \quad (3)$$

where i is the imaginary operator, t is time, $\text{amp}_{f2}(t)$ is the magnitude of the convolution result, or amplitude, of $f2$, $\varphi_{f1}(t)$ is the phase of $f1$, and B is the mean phase bias:

$$B = \frac{1}{n} \sum_{t=1}^{n} e^{i\varphi_{f1}(t)} \quad (4)$$

For same-site PAC (i.e., within HPC or within AMY) φ_{f1} and amp_{f2} stemmed from the same channel, whereas cross-site PAC used phase information from one brain structure and amplitude information from the other. For every 60-s segment, frequency pair, and same/cross-site combination, we constructed a surrogate distribution of coupling strengths by repeatedly ($n = 100$) time shifting the $f1$ phase time series with respect to the $f2$ amplitude time series and recalculating the mean vector length for each iteration. We then z-scored the observed coupling strength with respect to this null distribution of coupling strength values to obtain dPAC_Z, as shown in subpanels v of Figures 5 and 6.

Ripple Detection and Surrogates

NREM channel data were zero-phase band-pass filtered between 70 and 110 Hz with 5-Hz transition zones. The ripple envelope was calculated as the magnitude of the Hilbert-transformed filtered signal. Whenever the z-scored envelope exceeded an upper threshold of 2.5, a potential ripple was detected, while crossings of a lower threshold of 2 before and after this point marked the beginning and end, respectively, of the ripple. Start and end points were required to be at least 35 ms apart, corresponding to approximately 3 full cycles at 70 Hz. Ripple events that did not contain a minimum of 0.75 s of clean data on either side (corresponding to 1.5-s window lengths for co-occurrence and time-locking analyses) were discarded. Duration, maximum amplitude of ripple-filtered signal, and frequency of each ripple were determined, as was ripple density (number per minute).

For each patient and channel, we constructed 1000 distributions of "surrogate ripples," with each distribution containing as many surrogate ripples as detected ripples. Specifically, each surrogate ripple was defined as a random time point within

the NREM record, provided that this time point had a minimum of 0.75 s of clean data on either side, and that this extended 1.5-s window did not overlap with a true ripple's 1.5-s window. Note that while this approach allows overlapping data windows between surrogate ripples, the exact samples used for surrogate co-occurrence and time-locking analyses will seldomly overlap. Also note that because surrogates do not include (detected) ripple events, they necessarily differ from true ripples in their high-frequency content. While this makes certain statistical findings involving ripple frequencies trivial, it does not invalidate findings for other spectral components.

Ripple Co-occurrence

For both AMY and HPC channels, and for each detected ripple, we counted a co-occurrence when that ripple's maximum occurred within an interval (1.5 s, 500 ms, or 100 ms) surrounding any ripple maximum in the other channel. Surrogate co-occurrence rates were determined between a channel's true ripples and each of the 1000 surrogate ripple distributions from the other channel.

Ripple-Locked Analyses

All local and interregional ripple-related dynamics considered a 1.5-s analysis window centered on the ripple maximum and the 1000 distributions of surrogate ripples. Event-related potentials (subpanels i of Figs 5 and 6) were determined by averaging mean-centered ripple trials. The same procedure was used for each surrogate distribution, and the resulting distribution of surrogate ERPs was used to determine the 95% confidence interval at each time point. True and surrogate ERPs were further subjected to spectral analysis (Welch: window length 1.25 s, overlap 95%, spectral resolution 0.488 Hz), and ripple-related ERP power was visualized in raw and surrogate-normalized formats (subpanels *ii* of Figs 5 and 6).

Time-frequency power (squared magnitude of convolution result) was first normalized (z-scored) relative to all NREM sleep, followed by averaging across ripple-centered trials. This procedure was repeated for each surrogate distribution, and the true mean ripple-related power response was z-scored relative to the 1000 mean surrogate responses (subpanels *iii* of Figs 5 and 6). Time-frequency-resolved ITPC (subpanels *iv* of Figs 5 and 6) was determined similarly, both across true ripple trials and each distribution of surrogate trials, followed by z-scoring. Calculations followed equation (2), but using absolute phases instead of phase differences, and averaging across trials rather than time.

Statistical Analysis

With the exception of group-level comparisons of ripple properties (paired *t* test), statistical analyses were performed at the individual level. Significance of ripple co-occurrence was assessed by determining the proportion of surrogate co-occurrence rates that were identical or larger than the observed co-occurrence rate. Reliability of ripple-locked ERPs may be assessed by comparing their amplitude to the 95% confidence interval across surrogate ERPs. ERP-based power spectra are shown both in raw format and z-scored relative to surrogate ERP spectra, with a one-to-one mapping between z-scores and *P* values (e.g., z-scores of 2, 3, and 5 correspond to one-sided *P* values of ca., 0.02, 0.001, and 10^{-7}, respectively).

Ripple-locked power and ITPC responses, normalized to surrogate distributions, often yielded very high z-scores (particularly for local ripple-band responses). Hence, rather than evaluating significance at a single statistical threshold, cluster outlines were determined at a maximum of 5 integer z-values, ranging between the lowest $Z \geq 3$ not resulting in a cluster comprising all frequency bands, and the highest $Z \leq 25$ still generating a cluster. Clusters were required to span at least two-frequency bins and 10 time bins (36 ms). Note that $Z = 5$ corresponds to strict Bonferroni correction for a two-sided test across all time-frequency points ($0.025/18\,850 \approx 10^{-6}$).

The presence of PAC was assessed using cluster-based permutation tests (Maris and Oostenveld 2007) with a *clusteralpha* value of 0.1 and 1000 random permutations. Specifically, $dPAC_Z$ values at each frequency pair were compared to zero across data segments using one-tailed *t* tests (only above-zero effects are of interest). Clusters were required to span at least 2×2 frequency bins, and were deemed significant at $P < 0.05$ (one-tailed).

Of note, variable amounts of continuous data, and variable numbers of detected ripples, imply differential statistical power. Consequently, patients/channels with more data tend to show stronger effects (e.g., larger z-scores and cluster extents for p4). Although limiting analyses to identical amounts of data across patients addresses this issue, we did not wish to discard valuable data (e.g., 95% of p4's HPC ripples should be removed to match p2's number of AMY ripples), particularly in light of our small sample. Alternatively, we could have pooled ripple events across patients, but decided against this due to unequal contributions from each patient. It is in light of these considerations that we present data on an individual basis with variable data-derived statistical thresholds.

Data Availability

Data are not publicly available due to privacy concerns related to clinical data, but data are available from the corresponding or senior author upon obtaining ethical approval.

Code Availability

All computer code used to analyze data is available from the corresponding author on request.

Results

We analyzed invasive EEG during NREM (N2 and N3) sleep from 4 patients (p1–p4) suffering from intractable epilepsy implanted with multi-contact depth electrodes (patient details in Supplementary Table 1). Overnight sleep architecture calculated from scalp-based polysomnography indicated normal amounts of N2, but reduced proportions of N3 and REM sleep (Table 1). We determined bipolar activity from pairs of adjacent contacts located within nonpathological HPC and AMY, as assessed by clinical monitoring and individual anatomy (Fig. 1), ensuring spectral components are generated locally within each brain structure. Due to the limited sample size, group analyses were generally not possible; instead statistical analyses were performed at the single-subject level (see section *Statistical Analysis*). However, data interpretation is based on the agreement across patients.

Spectral Power and Functional Connectivity

We first sought to characterize the spectral components present within HPC and AMY during NREM sleep. Group-level spectra

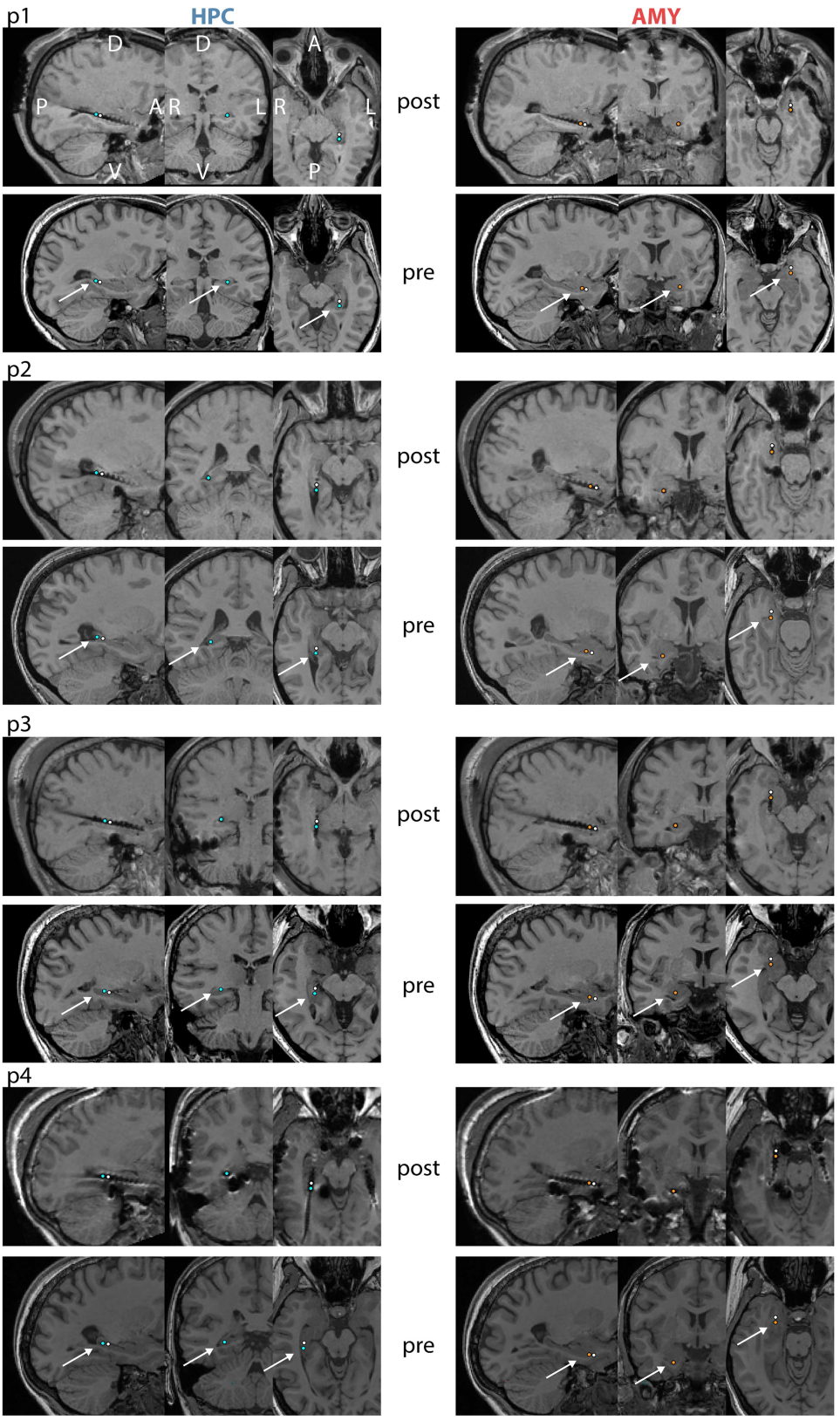

Figure 1. Electrode locations for individual patients. For each patient, top and bottom panels show co-registered post- and preimplantation T1-weighted MRI scans, respectively. Selected HPC contacts are indicated in left panels (blue: active, white: reference) and selected AMY contacts are shown in right panels (orange: active, white: reference). A: anterior, P: posterior, D: dorsal, V: ventral, L: left, R: right.

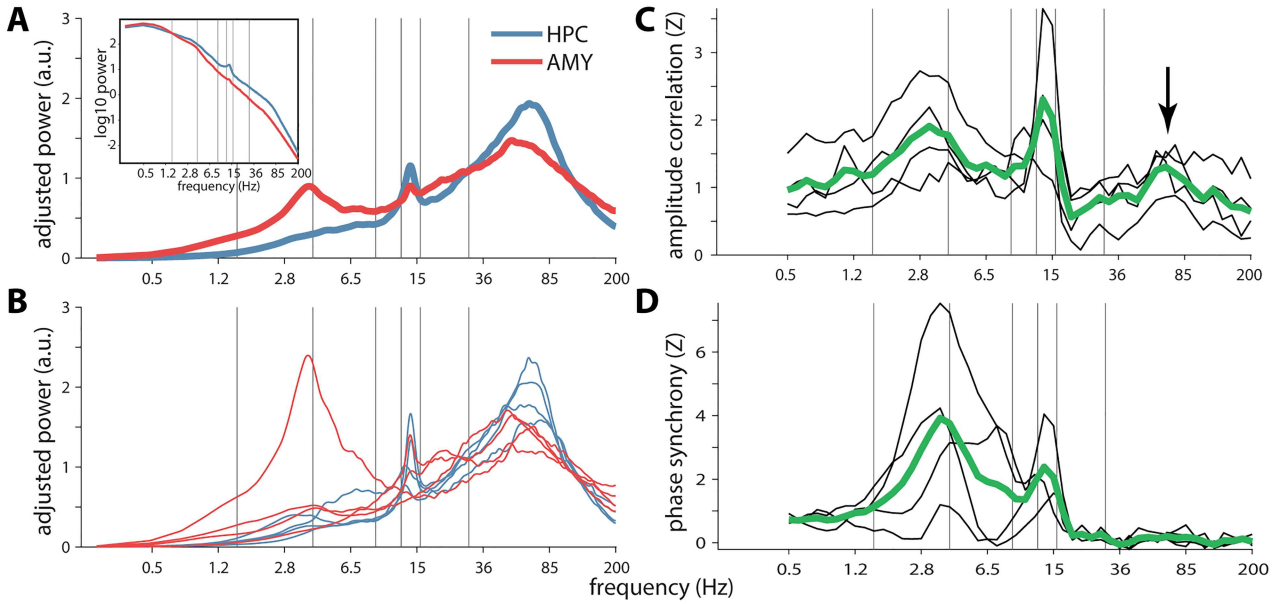

Figure 2. Power and functional connectivity spectra in/between hippocampus and amygdala. (*A*) Group-level slope-adjusted (main) and raw (inset) spectra. (*B*) Individual patients' slope-adjusted spectra. (*C*) Amplitude envelope correlations between HPC and AMY across patients (green) and for individual patients (black), normalized relative to surrogate distributions. Arrow indicates ripple-band connectivity. (*D*) Phase synchrony, normalized to surrogate distributions. Gray vertical lines at 1.5, 4, 9, 12.5, 16, and 30 Hz indicate approximate boundaries between SO, delta, theta, slow spindle, fast spindle, beta, and faster activity.

Table 1. Sleep architecture

	Mean	SD
N1 (%)	27.1	15.9
N2 (%)	45.1	10.6
N3 (%)	11.8	7.5
REM (%)	15.9	5.0
N1 (min)	142.1	90.1
N2 (min)	233.3	69.6
N3 (min)	59.3	34.2
REM (min)	80.2	21.8
Total sleep (min)	514.9	72.3
WASO (min)	70.6	79.3
Sleep efficiency (%)	88.1	12.7

Notes: WASO: wake after sleep onset; Sleep efficiency: percentage of recording time spent asleep.

adjusted for 1/f scaling showed broad spectral peaks in the 50–100 Hz range for both HPC and AMY (Fig. 2A), comprising the human ripple range (Staresina et al. 2015; Cox et al. 2019). Importantly, these putative ripple peaks were consistently present across patients for both brain structures (Fig. 2B), providing a first indication that ripples may be present in human AMY. Additionally, spindle peaks were present in all 4 patients for HPC, and in 2 patients for AMY, consistent with earlier indications of human AMY spindles (Andrillon et al. 2011; Muñoz-Torres et al. 2018). SO and SPW components were not strongly represented in the adjusted or raw spectra (Fig. 2A, inset) of either brain site, except for an individual with a prominent 4-Hz AMY peak.

Next, we assessed whether activity in any spectral band is coordinated between HPC and AMY, employing 2 mathematically and theoretically (but see Palva et al. 2018) independent forms of frequency-resolved functional connectivity. Surrogate-normalized AMY–HPC amplitude envelope correlations (Fig. 2C) and phase synchrony (Fig. 2D) signaled robust communication in the SPW (2–6 Hz) and spindle (12–16 Hz) ranges, indicating that activity in these frequency bands both co-occurs and is phase locked between these brain sites. Importantly, amplitude correlations also peaked in the 50–100-Hz range comprising the ripple band (arrow), suggesting that ripples tend to co-occur between these structures, though with variable phase relations as evident from the lack of phase synchrony.

Raw Traces and Spectrograms

Given these initial indications of AMY ripples and their coordination with their HPC counterparts, we visually examined raw HPC and AMY traces along with their spectrograms. This revealed brief (<100 ms) bursts of high-frequency activity in both brain structures centered on the 70–85-Hz range (Fig. 3A and B, left). Importantly, many of these events coincided with clear oscillatory behavior in the raw traces (Fig. 3A and B, right). Moreover, ripples in both structures were often superimposed on large deflections in the EEG, consistent with SPW-ripple complexes. Interestingly, while HPC and AMY increases in ripple-frequency power were mostly dissociated, instances of co-occurring ripple activity across these brain structures were also observed (Fig. 3B). Moreover, ripples in one site were sometimes associated with SPW-like activity at the other site (e.g., AMY ripple occurring in trough of putative HPC SPW; Fig. 3B). These visual observations, which were similar in the other patients, further suggest the existence of AMY ripples, their association with SPWs, and their coordination with HPC activity.

Ripple Characteristics

To examine these possibilities more objectively, we identified ripples using an automated detector (examples for patient p1 in Fig. 4; examples for other patients in Supplementary Figs 1–3). Across patients, we detected a grand total of 2196 HPC

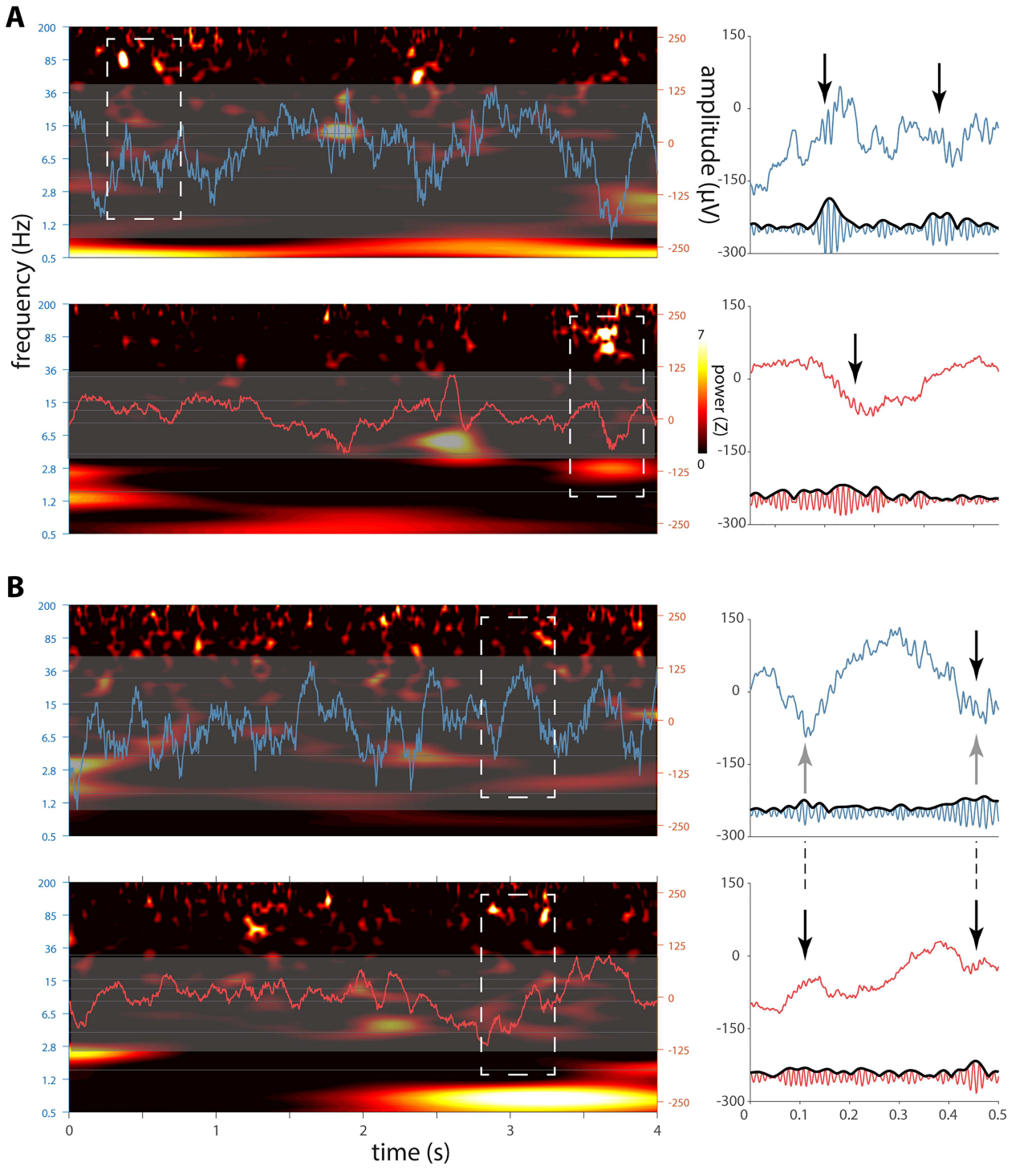

Figure 3. Sleep electrophysiology in hippocampus and amygdala for patient p1. Left panels in (*A*) and (*B*) each show 4-s segments of concurrent HPC (top, blue) and AMY (bottom, red) raw traces overlaid on spectrograms (*z*-scored relative to all NREM sleep). Note brief increases of ~80-Hz power at both brain sites. Close-ups of dashed rectangles in right panels indicate ripple-band oscillatory activity in raw (top) and 70–110-Hz filtered (bottom) traces (black arrows: putative ripples), with (*A*) showing independent HPC and AMY ripples and (*B*) showing AMY ripples co-occurring with both a HPC ripple and putative HPC–SPWs (gray arrows).

and 979 AMY ripple events. Average ripple density (number per minute) in HPC was consistent with previous human reports (Staresina et al. 2015) and about twice that of AMY (5.5 ± 1.7 vs. 2.6 ± 1.0; paired *t* test: $t(3) = 5.8$, $P = 0.01$). Ripple duration (47.9 ± 1.9 vs. 47.1 ± 1.7 ms; $t(3) = 0.7$, $P = 0.52$), main frequency (79.9 ± 1.0 vs. 80.0 ± 1.1 Hz; $t(3) = -0.2$, $P = 0.86$), and amplitude (12.1 ± 5.7 vs. 6.3 ± 1.6 μV; $t(3) = 1.8$, $P = 0.17$) did not differ systematically between HPC and AMY, although ripple amplitudes differed between sites on a within-patient basis (Table 2).

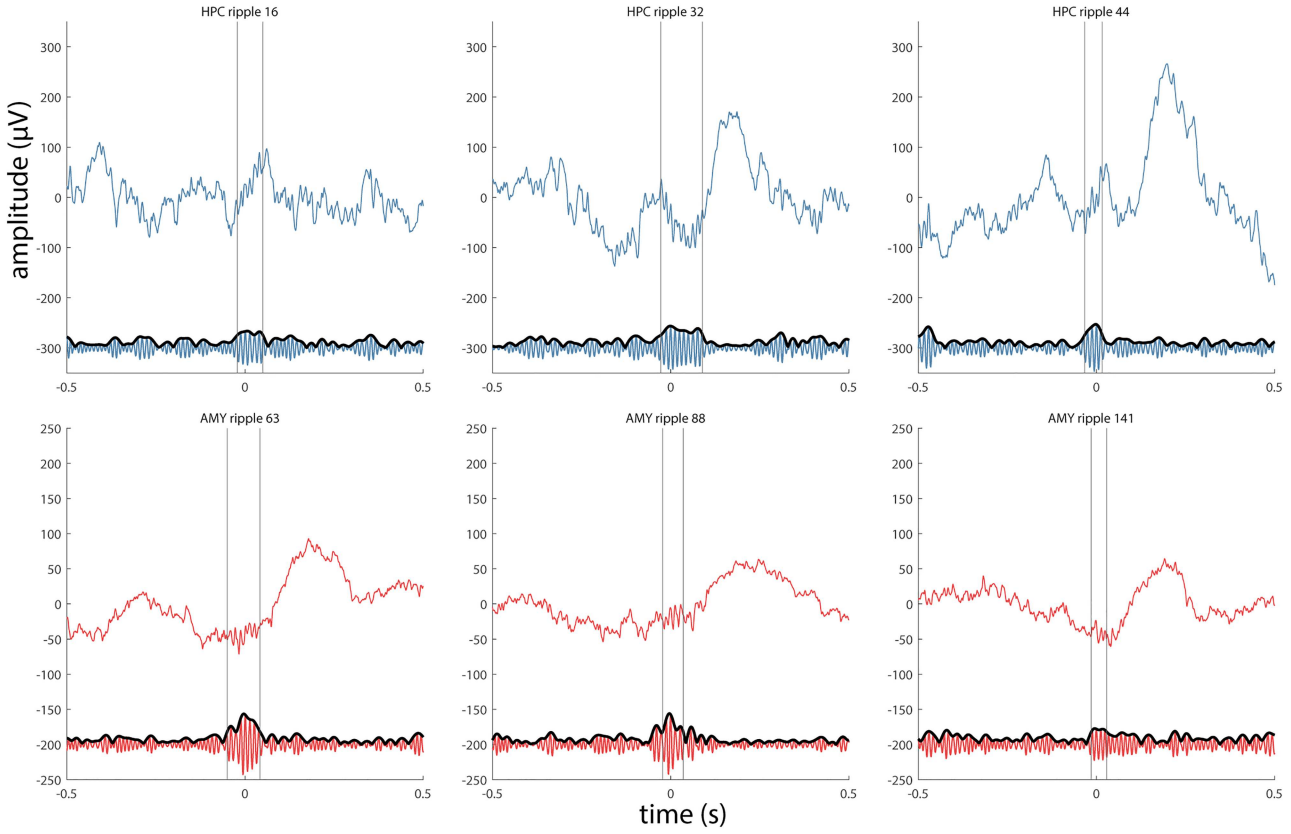

Figure 4. Examples of detected ripples for patient p1. Three HPC ripples (top panels, blue) and 3 AMY ripples (bottom panels, red) are shown as raw signal (top trace) and in the ripple-filtered (70–110 Hz) band (bottom trace). Vertical lines indicate start and end of ripple.

Table 2. Ripple characteristics for individual patients

	Number	Density (per min)	Duration (ms)	Main frequency (Hz)	Amplitude (μV)
p1					
HPC	353	6.2	47.6 ± 11.6	79.6 ± 6.6	19.3 ± 3.5
AMY	163	2.9	44.9 ± 11.8	81.2 ± 8.4	6.6 ± 1.4
t-test *P*			0.01	0.02	0*
p2					
HPC	225	3.3	45.8 ± 11.4	79.3 ± 7.2	12.4 ± 1.7
AMY	76	1.1	47.8 ± 11.6	78.7 ± 7.9	4.1 ± 1.1
t-test *P*			0.19	0.49	0*
p3					
HPC	221	5.2	50.4 ± 16.6	81.3 ± 8.4	5.3 ± 1.3
AMY	138	3.3	48.8 ± 12.6	80.6 ± 8.7	7.7 ± 2.0
t-test *P*			0.32	0.46	0*
p4					
HPC	1397	7.2	47.6 ± 13.1	79.3 ± 7.7	11.4 ± 2.0
AMY	602	3.1	47.1 ± 12.0	79.5 ± 8.2	7.0 ± 1.5
t-test *P*			0.42	0.56	0*

Notes: Results of HPC/AMY comparisons (independent *t*-tests, uncorrected) are shown.
*P value smaller than available numerical precision.

Next, we investigated whether HCP and AMY ripple events tend to co-occur. We calculated the proportion of the more abundant HPC ripples that co-occurred with the less frequent AMY ripples. Parametrically varying window length, we found relatively low co-occurrence rates of 23.5 ± 6.6 (1500 ms), 11.2 ± 3.4 (500 ms), and 5.0 ± 1.9% (100 ms), indicating that HPC and AMY ripples at the employed recording sites are mostly dissociated. Nonetheless, these co-occurrence rates were significantly enriched relative to surrogate distributions (permutation tests; p1: all $P < 0.03$; p2: all $P < 0.12$; p3: all $P < 0.003$; p4: all $P < 0.001$). As expected, co-occurrences in the opposite direction were lower (11.9 ± 4.4, 5.4 ± 1.9, and 2.4 ± 1.0%, respectively), reflecting the lower ripple density in AMY, but generally still higher than chance (Table 3). Pooled

Table 3. Ripple co-occurrence rates for individual patients

	Window (ms)		1500	500	100
p1	HPC during AMY	%	25.2	11.0	4.3
		P	0.001	0.024	0.007
	AMY during HPC	%	10.5	4.5	2.0
		P	0.11	0.11	0.02
p2	HPC during AMY	%	14.5	6.6	2.6
		P	0.06	0.11	0.10
	AMY during HPC	%	5.3	2.7	0.9
		P	0.07	0.06	0.11
p3	HPC during AMY	%	21.7	10.9	5.1
		P	0.003	0.004	<0.001*
	AMY during HPC	%	16.7	7.2	3.2
		P	<0.001*	0.004	0.001
p4	HPC during AMY	%	32.7	16.3	8.0
		P	<0.001*	<0.001*	<0.001*
	AMY during HPC	%	15.1	7.2	3.4
		P	<0.001*	<0.001*	<0.001*

Notes: *P* values (uncorrected) for permutation tests relative to 1000 distributions of surrogate ripples.
*Observed ripple co-occurrence was higher than all surrogate iterations.

across all patients' precise (100-ms window) co-occurrences, ripple timing differences between HPC and AMY did not reliably differ from zero (4.1 ± 28.6 ms; $t(63) = 1.1$, $P = 0.26$). Overall, these findings indicate that a subset of ripples occurs synchronously between HPC and AMY, consistent with the ripple-band envelope correlations of Figure 2C.

Ripple-Related Dynamics in HPC and AMY

Next, we investigated whether detected ripple events in either structure are temporally associated with other electrophysiological phenomena (e.g., SPWs, spindles, SOs), and if so, which ones. We examined each patient's ripple-related dynamics locally within HPC and AMY using 5 complementary approaches (example patient in Fig. 5; other patients in panels AB of Supplementary Figs 4–6). Because patients showed heterogeneous effects, we limit interpretation to those results present in at least half of the sample.

First, we time locked the raw signal to the maxima of detected ripples, akin to event-related potential (ERP) analyses (Fig. 5, subpanels *i*). Ripples in both HPC and AMY occurred against a background of large-amplitude fluctuations consistent with SPWs, confirming the individual ripple observations of Figure 3. These deflections were reliably greater than expected by chance, as indicated by 95% confidence intervals (gray) across 1000 surrogate ERPs centered on nonripple events. Importantly, HPC and AMY ripple-related SPW activity was seen for each patient ($N = 4$), although precise timing and polarity varied, the latter likely due to bipolar referencing.

Second, examination of power spectra for these ripple-centered ERPs revealed strong peaks in the 2–8-Hz SPW range ($N = 4$), with these SPW peaks being much more pronounced relative to spectra derived from surrogate ERPs (Fig. 5, subpanels *ii*).

Third, we evaluated ripple-triggered time-frequency power relative to surrogate distributions (Fig. 5, subpanels *iii*). Unsurprisingly, for both HPC and AMY, this yielded strong enhancements in ripple-frequency power around the time-locking moment for each patient. Clear increases in 2–8-Hz power surrounding AMY ($N = 2$) and HPC ($N = 2$) ripple detection were also apparent, again consistent with SPW activity. In addition, distinct clusters of spindle power enhancement during or immediately following ripples were seen for AMY ($N = 2$). For HPC, only one patient showed a clear spindle cluster, although an additional patient showing a more broadband power increase comprising the spindle range. Overall, these findings indicate that both SPW and spindle activity tend to occur in close proximity to ripple oscillations, in both AMY and HPC.

The ERP findings from subpanels i suggest that ripples preferentially occur at a specific phase of the SPW. Fourth, therefore, we examined time-frequency-resolved intertrial phase clustering (ITPC) across ripple trials, relative to surrogate distributions (Fig. 5, subpanels *iv*). Aside from expected cross-trial phase locking in the ripple band, this analysis indicated consistently phase-aligned activity in the 2–8-Hz range surrounding the ripple maximum for in both HPC ($N = 4$) and AMY ($N = 4$), indicating that ripples are reliably tied to a specific SPW phase. More consistent SPW effects for ITPC than power suggest that some patients' SPWs do not exceed immediately preceding and following amplitude fluctuations at delta/theta frequencies, but nevertheless powerfully modulate ripple expression. In addition, we observed clusters of enhanced spindle/beta ITPC around and before the ripple maximum for HPC ($N = 2$) and AMY ($N = 1$), with an additional patient showing larger clusters comprising the spindle range at both sites, further underscoring the relation between ripple and spindle activity.

The preceding indications for ripples being associated with SPWs and spindles are all relative to algorithmically identified ripples, requiring ultimately subjective detection criteria. Previous reports have shown that SPW-ripple activity is also reflected by phase-amplitude coupling (PAC) metrics calculated from continuous data (Staresina et al. 2015; Cox et al. 2019, 2020), while further allowing the identification of other coupling phenomena. Fifth, therefore, we constructed surrogate-normalized comodulograms from continuous data, indicating the degree of PAC for every frequency pair in the 0.5–200-Hz range (Fig. 5, subpanels *v*). While clusters emerged for various frequency pairs as reported previously for HPC and NC (Cox et al. 2019, 2020), ripple-band amplitudes in both HPC ($N = 4$) and AMY ($N = 4$) depended strongly on the phase of ~3–6-Hz activity. This is further illustrated by traces at the bottom of each comodulogram, indicating that ripple-band activity is typically coupled most strongly to the

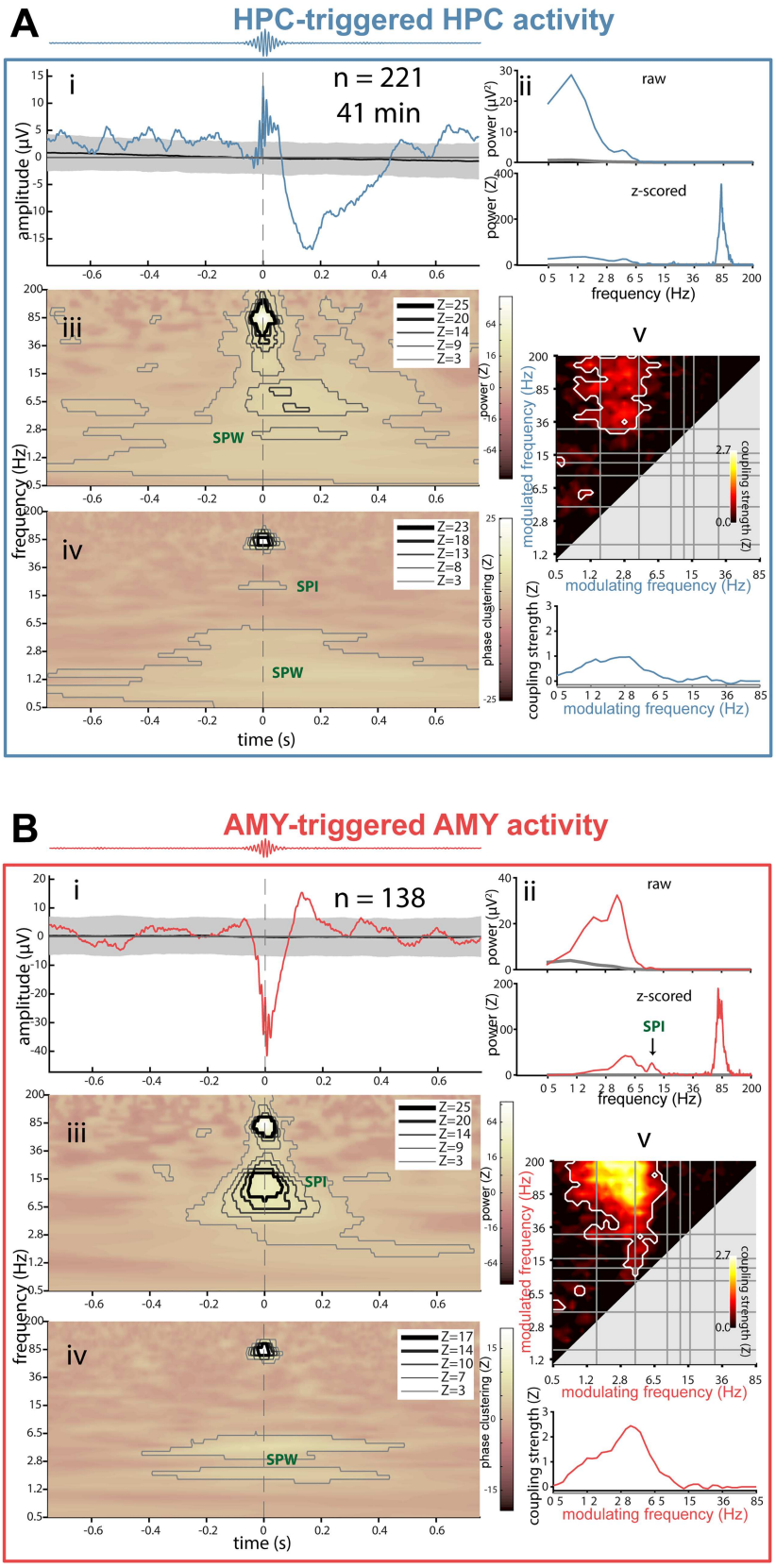

Figure 5. Local ripple-related dynamics in hippocampus and amygdala for patient p3. (A) HPC activity relative to HPC ripples. (B) AMY activity relative to AMY ripples. Subpanels indicate (i) ripple-triggered ERP (colored) and 95% confidence interval across 1000 surrogate ERPs, each based on surrogate ripples. (ii) Power spectra of ERPs from (i), with top panel showing raw spectra from ripple ERP (colored) and mean across surrogate ERPs (gray), and bottom panel showing z-scored spectrum (colored) relative to surrogate-based ERP spectra (gray: $z = 0$). SPW peaks are visible in both panels, with additional ripple (A) and (B), and spindle peaks only visible in z-scored spectra. (iii) Ripple-triggered time-frequency power, z-scored relative to surrogates. Contour lines indicate significant clusters at different levels of significance (Z of 3 and 5 corresponding to P of ca., 0.001 and 10^{-7}, respectively). Color scale square root transformed to accommodate strong ripple clusters. (iv) Ripple-triggered time-frequency intertrial phase clustering. z-scored relative to surrogates. Clusters as in (iii). (v) Top: comodulogram of cross-frequency phase-amplitude coupling calculated from continuous data, z-scored relative to time-shifted surrogates. White outlines indicate clusters of significantly higher than zero coupling across 1-min data segments ($P < 0.05$, cluster-based permutation test). Bottom: modulation of ripple-range (wavelet center frequencies: 75–110 Hz) activity by slower frequencies (0.5–85 Hz).

phase of delta/theta frequencies, with additional modulation sometimes exerted by the SO and spindle bands.

Combined, these findings establish that human ripples in both HPC and AMY occur in close temporal proximity to, and are phase coordinated with, local SPWs, and to a lesser extent, sleep spindles.

Ripple-Related Dynamics Between HPC and AMY

Having characterized ripple-related dynamics locally within HPC and AMY, we turned to cross-regional analyses to determine whether ripple events at one site are temporally associated with electrophysiological phenomena at the other site. Adopting the same analysis strategy as employed in the previous section, we time locked the raw AMY signal to HPC ripples (Fig. 6A, subpanel *i*) and the HPC signal to AMY ripples (Fig. 6B, subpanel *i*; other patients in panels CD of Supplementary Figs 4–6). This cross-regional analysis again yielded ripple-locked amplitude fluctuations consistent with SPWs in most instances (AMY-locked: $N = 4$; HPC-locked: $N = 3$), although with smaller amplitudes (relative to both surrogate ERPs and the local analyses from the previous section). A similar picture emerged from ERP-based power analyses, again expressing clear peaks in the SPW range in most cases (Fig. 6, subpanels *ii*). Importantly, for 3 out of 4 patients, these effects were present in both directions, suggesting both HPC–AMY and AMY–HPC crosstalk.

Cross-regional ripple-centered time-frequency power analyses (Fig. 6, subpanels *iii*) indicated significant ripple power enhancements at both sites during ripples in the other region ($N = 2$), supporting the earlier ripple-band amplitude correlations and co-occurrence analyses. In contrast, no interregional ripple-band ITPC was seen for these patients (Fig. 6, subpanels *iv*), consistent with the lack of ripple phase synchrony from Fig. 2D. However, for each patient, either SPW power or SPW ITPC was enhanced in at least one direction, suggesting that ripples at one site are associated with SPWs at the other site. Likewise, interregional comodulogram analyses of continuous data indicated strong bidirectional PAC between the phase of delta/theta frequencies and power in the ripple band (Fig. 6, subpanels *v*), further confirming coordinated SPW-ripple activity across HPC and AMY.

Discussion

While accumulating behavioral evidence indicates a role for NREM sleep in emotional processing (Hauner et al. 2013; Cairney et al. 2014, 2015; Cellini et al. 2016; Lehmann et al. 2016; Cox et al. 2018), it has remained unclear how these processes are implemented neurophysiologically. We report both the existence of SPW-ripples in AMY, and bidirectional electrophysiological AMY–HPC interactions centered on ripple activity during NREM sleep, potentially underlying these behavioral findings.

We demonstrate the presence of ~80-Hz ripple oscillations in human AMY, as indicated by converging evidence from visual examinations, power and functional connectivity spectra, and event detection methods. While this observation is broadly consistent with high-frequency (>120 Hz) ripples in animal AMY (Ponomarenko et al. 2003; Haufler and Pare 2014) and fits with the frequency range of human HPC ripples (Bragin et al. 1999; Axmacher et al. 2008; Staresina et al. 2015), ripples have not yet been reported in human AMY. The first question is whether it is appropriate to employ the term "ripples" for these observations, as SPW-ripples are typically defined in terms of their HPC subfield and laminar generators (Buzsáki 2015). On the other hand, ripples have been described in human NC regions both close and distant to HPC (Clemens et al. 2007; Axmacher et al. 2008; Zhang et al. 2018; Vaz et al. 2019). Moreover, given that our detected AMY and HPC ripple events had highly similar spectral compositions and durations, and were similarly associated with local and interregional SPWs, we believe these AMY events may reasonably be categorized as ripples.

HPC SPW-ripples are strongly associated with the replay of task-related firing sequences and subsequent memory consolidation (Wilson and McNaughton 1994; Girardeau et al. 2009). Combined with replay events in AMY (Girardeau et al. 2017), a plausible scenario is that AMY SPW-ripples organize the recapitulation of waking experiences' affective components. In this light, it is noteworthy that HPC and AMY ripple co-occurrence was modest, suggesting mostly independent reactivation processes at the employed recording sites. Here, it may be noted that patients did not engage in a presleep emotional task, which might have increased ripple co-occurrences. Still, co-occurrence rates were higher than chance, allowing for integrated AMY–HPC replay, as further supported by ripple-band amplitude correlations (Fig. 2C) and cross-regional ripple power increases (Fig. 6, subpanels *iii*).

Besides their strong linkage to local SPWs, ripples in AMY and HPC were also reliably associated with SPWs at the other site, expressed as both loose temporal associations and precise phase-amplitude coupling. Similarly, SPW activity was itself coordinated between brain sites, as evidenced by strong enhancements in SPW-band functional connectivity in terms of both amplitude and phase (Fig. 2C and *D*). Overall, these findings indicate that ripples and SPWs, both in isolation and as part of SPW-ripple complexes, are coordinated between HPC and AMY during NREM sleep.

Interestingly, spindles emerged as another oscillatory component mediating AMY–HPC coordination. Irrespective of ripples, both amplitude- and phase-based spindle activity were consistently coordinated across patients between AMY and HPC (Fig. 2C and *D*). These findings extend observations of spindle synchrony between HPC and NC (Helfrich et al. 2019; Cox et al. 2020), or within NC (Cox et al. 2014), involving AMY in a widespread network of spindle-related coordination. Moreover, we observed several instances in which ripples were associated with locally enhanced spindle activity in both AMY and HPC. In contrast, evidence for local or interregional spindle-ripple PAC was generally absent. Finally, it deserves mention that no consistent evidence for SO-related AMY–HPC communication emerged, either viewed on its own (Fig. 2C and *D*) or in conjunction with ripples (i.e., no ripple-related SO power or ITPC increases). However, this could be related to the fact that our data contained relatively little SO-rich N3 sleep.

Aside from our choice for local referencing, empirical findings of 1) relatively low ripple co-occurrence, 2) low interregional ripple-band phase synchrony (Fig. 2D), and 3) low interregional ripple-band ITPC (Fig. 6, subpanels *iv*), essentially rule out that AMY SPW-ripples and interregional AMY–HPC communication are due to volume conduction or a common referential signal.

A limitation of the present study is its small sample size, which is a consequence of our desire to capture local signals from HPC and AMY. This required 2 relatively distant (4.5 mm center-to-center) electrode contacts to be unambiguously localized within each brain site, which proved relatively rare for the small AMY structure. While our sample size is not atypical for human invasive sleep studies (Cantero et al. 2003, 2004; Mak-McCully et al. 2017; Muñoz-Torres et al. 2018), this situation

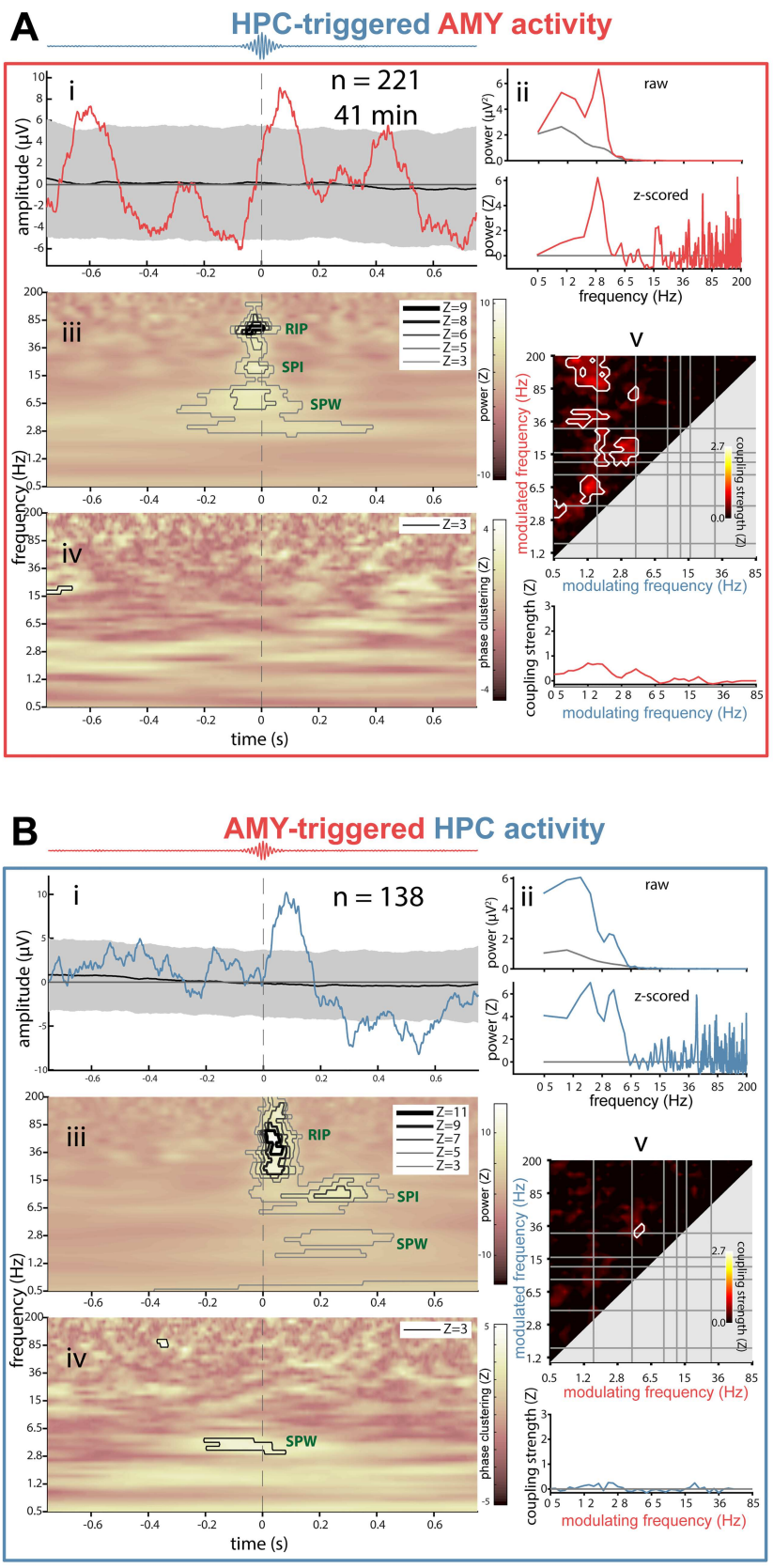

Figure 6. Interregional ripple-related dynamics between hippocampus and amygdala for patient p3. (*A*) AMY activity relative to HPC ripples. (*B*) HPC activity relative to AMY ripples. Subpanels as in Figure 5. For comodulograms (subpanel *iv*): phase of modulating frequency (*x*-axis) from time-locking (triggered) site (i.e., modulation of AMY activity by HPC phase in (*A*).

prevented traditional group statistics. Instead, we performed rigorous surrogate-based single-subject analyses, and limited interpretations to those effects occurring in at least half of our sample. Overall, evidence for local and interregional SPW-ripples was surprisingly consistent across patients, while linked ripple-spindle activity was also seen in half of our patients. In contrast, various heterogeneous effects (Figs 5 and 6, Supplementary Figs 4–6) require confirmation in a larger sample.

Patients in our sample exhibited insufficient clean REM sleep data to examine AMY–HPC communication in this brain state, which has also been implicated in emotional (memory) processing (Wagner et al. 2001; Nishida et al. 2009; Baran et al. 2012; Payne et al. 2012; Groch et al. 2013; Wiesner et al. 2015). But while REM sleep harbors both HPC replay (Louie and Wilson 2001) and enhanced hemodynamic AMY activity (Maquet et al. 1996), the paucity of SPW-ripples (Staba et al. 2004; Buzsáki 2015), replay events (Girardeau et al. 2017), and spindles during this brain state suggest that any such coordination would have to be implemented differently from the one reported here for NREM sleep. Future work should delineate whether and how ripple characteristics, their co-occurrences, and their linkage to local and interregional SPWs and spindles, are modulated by presleep emotional experiences, or relate to overnight changes in affective (memory) processing.

To conclude, we present first evidence for the existence of AMY SPW-ripples and their coordination with HPC activity. These findings offer an attractive physiological basis for a large body of findings implicating human sleep, and NREM sleep in particular, in the regulation and consolidation of emotional content.

Supplementary Material

Supplementary material can be found at *Cerebral Cortex Communications* online.

Funding

The German Research Foundation (FE366/9-1 to J.F.); a Wellcome Trust/Royal Society Sir Henry Dale Fellowship (107672/Z/15/Z to B.P.S.).

References

Andrillon T, Nir Y, Staba RJ, Ferrarelli F, Cirelli C, Tononi G, Fried I. 2011. Sleep spindles in humans: insights from intracranial EEG and unit recordings. *J Neurosci*. **31**:17821–17834.

Axmacher N, Elger CE, Fell J. 2008. Ripples in the medial temporal lobe are relevant for human memory consolidation. *Brain*. **131**:1806–1817.

Baran B, Pace-Schott EF, Ericson C, Spencer RMC. 2012. Processing of emotional reactivity and emotional memory over sleep. *J Neurosci*. **32**:1035–1042.

Bragin A, Engel J, Wilson CL, Fried I, Buzsáki G. 1999. High-frequency oscillations in human brain. *Hippocampus*. **9**:137–142.

Bruns A, Eckhorn R, Jokeit H, Ebner A. 2000. Amplitude envelope correlation detects coupling among incoherent brain signals. *Neuroreport*. **11**:1509–1514.

Buzsáki G. 2015. Hippocampal sharp wave-ripple: a cognitive biomarker for episodic memory and planning. *Hippocampus*. **25**:1073–1188.

Cairney SA, Durrant SJ, Hulleman J, Lewis PA. 2014. Targeted memory reactivation during slow wave sleep facilitates emotional memory consolidation. *Sleep*. **37**:701–707.

Cairney SA, Durrant SJ, Power R, Lewis PA. 2015. Complementary roles of slow-wave sleep and rapid eye movement sleep in emotional memory consolidation. *Cereb Cortex*. **25**:1565–1575.

Canolty RT, Edwards E, Dalal SS, Soltani M, Nagarajan SS, Kirsch HE, Berger MS, Barbaro NM, Knight RT. 2006. High gamma power is phase-locked to theta oscillations in human neocortex. *Science*. **313**:1626–1628.

Cantero JL, Atienza M, Madsen JR, Stickgold R. 2004. Gamma EEG dynamics in neocortex and hippocampus during human wakefulness and sleep. *NeuroImage*. **22**:1271–1280.

Cantero JL, Atienza M, Stickgold R, Kahana MJ, Madsen JR, Kocsis B. 2003. Sleep-dependent theta oscillations in the human hippocampus and Neocortex. *J Neurosci*. **7**.

Cellini N, Torre J, Stegagno L, Sarlo M. 2016. Sleep before and after learning promotes the consolidation of both neutral and emotional information regardless of REM presence. *Neurobiol Learn Mem*. **133**:136–144.

Clemens Z, Molle M, Eross L, Barsi P, Halasz P, Born J. 2007. Temporal coupling of parahippocampal ripples, sleep spindles and slow oscillations in humans. *Brain*. **130**:2868–2878.

Cohen MX. 2019. A better way to define and describe Morlet wavelets for time-frequency analysis. *NeuroImage*. **199**:81–86.

Cox R, Rüber T, Staresina BP, Fell J. 2019. Heterogeneous profiles of coupled sleep oscillations in human hippocampus. *NeuroImage*. **202**:116178.

Cox R, Rüber T, Staresina BP, Fell J. 2020. Phase-based coordination of hippocampal and neocortical oscillations during human sleep. *Commun Biol*. **3**:176

Cox R, van Bronkhorst MLV, Bayda M, Gomillion H, Cho E, Parr ME, Manickas-Hill OP, Schapiro AC, Stickgold R. 2018. Sleep selectively stabilizes contextual aspects of negative memories. *Sci Rep*. **8**:17861.

Cox R, van Driel J, de Boer M, Talamini LM. 2014. Slow oscillations during sleep coordinate interregional communication in cortical networks. *J Neurosci*. **34**:16890–16901.

Dave S, Brothers TA, Swaab TY. 2018. 1/ f neural noise and electrophysiological indices of contextual prediction in aging. *Brain Res*. **1691**:34–43.

Delorme A, Makeig S. 2004. EEGLAB: an open source toolbox for analysis of single-trial EEG dynamics including independent component analysis. *J Neurosci Methods*. **134**:9–21.

Girardeau G, Benchenane K, Wiener SI, Buzsáki G, Zugaro MB. 2009. Selective suppression of hippocampal ripples impairs spatial memory. *Nat Neurosci*. **12**:1222–1223.

Girardeau G, Inema I, Buzsáki G. 2017. Reactivations of emotional memory in the hippocampus–amygdala system during sleep. *Nat Neurosci*. **20**:1634–1642.

Groch S, Wilhelm I, Diekelmann S, Born J. 2013. The role of REM sleep in the processing of emotional memories: evidence from behavior and event-related potentials. *Neurobiol Learn Mem*. **99**:1–9.

Haller M, Donoghue T, Peterson E, Varma P, Sebastian P, Gao R, Noto T, Knight RT, Shestyuk A, Voytek B. 2018. Parameterizing neural power spectra. *bioRxiv*. https://doi.org/10.1101/299859.

Haufler D, Pare D. 2014. High-frequency oscillations are prominent in the extended amygdala. *J Neurophysiol*. **112**:110–119.

Hauner KK, Howard JD, Zelano C, Gottfried JA. 2013. Stimulus-specific enhancement of fear extinction during slow-wave sleep. *Nat Neurosci*. **16**:1553–1555.

Helfrich RF, Lendner JD, Mander BA, Guillen H, Paff M, Mnatsakanyan L, Vadera S, Walker MP, Lin JJ, Knight RT. 2019. Bidirectional prefrontal-hippocampal dynamics organize information transfer during sleep in humans. *Nat Commun*. **10**:3572.

Jenkinson M, Beckmann CF, Behrens TEJ, Woolrich MW, Smith SM. 2012. FSL. *NeuroImage*. **62**:782–790.

Lachaux J-P, Rodriguez E, Martinerie J, Varela FJ. 1999. Measuring phase synchrony in brain signals. *Hum Brain Mapp*. **8**:194–208.

Latchoumane C-FV, Ngo H-VV, Born J, Shin H-S. 2017. Thalamic spindles promote memory formation during sleep through triple phase-locking of cortical, thalamic, and hippocampal rhythms. *Neuron*. **95**:424–435.e6.

Lehmann M, Schreiner T, Seifritz E, Rasch B. 2016. Emotional arousal modulates oscillatory correlates of targeted memory reactivation during NREM, but not REM sleep. *Sci Rep*. **6**:39229.

Logothetis NK, Eschenko O, Murayama Y, Augath M, Steudel T, Evrard HC, Besserve M, Oeltermann A. 2012. Hippocampal–cortical interaction during periods of subcortical silence. *Nature*. **491**:547–553.

Louie K, Wilson MA. 2001. Temporally structured replay of awake hippocampal ensemble activity during rapid eye movement sleep. *Neuron*. **29**:145–156.

Maingret N, Girardeau G, Todorova R, Goutierre M, Zugaro M. 2016. Hippocampo-cortical coupling mediates memory consolidation during sleep. *Nat Neurosci*. **19**:959–964.

Mak-McCully RA, Rolland M, Sargsyan A, Gonzalez C, Magnin M, Chauvel P, Rey M, Bastuji H, Halgren E. 2017. Coordination of cortical and thalamic activity during non-REM sleep in humans. *Nat Commun*. **8**:15499.

Maquet P, Péters J, Aerts J, Delfiore G, Degueldre C, Luxen A, Franck G. 1996. Functional neuroanatomy of human rapid-eye-movement sleep and dreaming. *Nature*. **383**:163–166.

Maris E, Oostenveld R. 2007. Nonparametric statistical testing of EEG- and MEG-data. *J Neurosci Methods*. **164**:177–190.

Martin R. 2001. Noise power spectral density estimation based on optimal smoothing and minimum statistics. *IEEE Trans Speech Audio Process*. **9**:504–512.

Miller KJ, Sorensen LB, Ojemann JG, den Nijs M. 2009. Power-law scaling in the brain surface electric potential. *PLoS Comput Biol*. **5**:e1000609.

Muñoz-Torres Z, Velasco F, Velasco AL, Del Río-Portilla Y, Corsi-Cabrera M. 2018. Electrical activity of the human amygdala during all-night sleep and wakefulness. *Clin Neurophysiol*. **129**:2118–2126.

Ngo H-V, Fell J, Staresina B. 2020. Sleep spindles mediate hippocampal-neocortical coupling during long-duration ripples. *elife*. **9**:e57011.

Nir Y, Staba RJ, Andrillon T, Vyazovskiy VV, Cirelli C, Fried I, Tononi G. 2011. Regional slow waves and spindles in human sleep. *Neuron*. **70**:153–169.

Nishida M, Pearsall J, Buckner RL, Walker MP. 2009. REM sleep, prefrontal theta, and the consolidation of human emotional memory. *Cereb Cortex*. **19**:1158–1166.

Norman Y, Yeagle EM, Khuvis S, Harel M, Mehta AD, Malach R. 2019. Hippocampal sharp-wave ripples linked to visual episodic recollection in humans. *Science*. **365**:eaax1030.

Palva JM, Wang SH, Palva S, Zhigalov A, Monto S, Brookes MJ, Schoffelen J-M, Jerbi K. 2018. Ghost interactions in MEG/EEG source space: a note of caution on inter-areal coupling measures. *NeuroImage*. **173**:632–643.

Payne JD, Chambers AM, Kensinger EA. 2012. Sleep promotes lasting changes in selective memory for emotional scenes. *Front Integr Neurosci*. **6**:108.

Payne JD, Kensinger EA. 2010. Sleep's role in the consolidation of emotional episodic memories. *Curr Dir Psychol Sci*. **19**:290–295.

Payne JD, Kensinger EA. 2011. Sleep leads to changes in the emotional memory trace: evidence from fMRI. *J Cogn Neurosci*. **23**:1285–1297.

Payne JD, Kensinger EA. 2018. Stress, sleep, and the selective consolidation of emotional memories. *Curr Opin Behav Sci*. **19**:36–43.

Payne JD, Stickgold R, Swanberg K, Kensinger EA. 2008. Sleep preferentially enhances memory for emotional components of scenes. *Psychol Sci*. **19**:781–788.

Ponomarenko AA, Korotkova TM, Haas HL. 2003. High frequency (200 Hz) oscillations and firing patterns in the basolateral amygdala and dorsal endopiriform nucleus of the behaving rat. *Behav Brain Res*. **141**:123–129.

Rechtschaffen A, Kales A. eds. 1968. A manual of standardized terminology, techniques and scoring system for sleep stages of human subjects. Los Angeles: Brain Information Service/Brain Research Institute, University of California.

Rings T, Cox R, Rüber T, Lehnertz K, Fell J. 2020. No evidence for spontaneous cross-frequency phase–phase coupling in the human hippocampus. *Eur J Neurosci*. **51**:14608.

Sheehan TC, Sreekumar V, Inati SK, Zaghloul KA. 2018. Signal complexity of human intracranial EEG tracks successful associative-memory formation across individuals. *J Neurosci*. **38**:1744–1755.

Silber MH, Ancoli-Israel S, Bonnet MH, Chokroverty S, Grigg-Damberger MM, Hirshkowitz M, Kapen S, Keenan SA, Kryger MH, Penzel T, et al. 2007. The visual scoring of sleep in adults. *J Clin Sleep Med*. **3**:121–131.

Smith SM. 2002. Fast robust automated brain extraction. *Hum Brain Mapp*. **17**:143–155.

Staba RJ, Wilson CL, Bragin A, Jhung D, Fried I, Engel J. 2004. High-frequency oscillations recorded in human medial temporal lobe during sleep. *Ann Neurol*. **56**:108–115.

Staresina BP, Bergmann TO, Bonnefond M, van der Meij R, Jensen O, Deuker L, Elger CE, Axmacher N, Fell J. 2015. Hierarchical nesting of slow oscillations, spindles and ripples in the human hippocampus during sleep. *Nat Neurosci*. **18**:1679–1686.

Sterpenich V, Albouy G, Darsaud A, Schmidt C, Vandewalle G, Dang Vu TT, Desseilles M, Phillips C, Degueldre C, Balteau E, et al. 2009. Sleep promotes the neural reorganization of remote emotional memory. *J Neurosci*. **29**:5143–5152.

Talamini LM, Bringmann LF, de Boer M, Hofman WF. 2013. Sleeping worries away or worrying away sleep? Physiological evidence on sleep-emotion interactions. *PLoS One*. **8**:e62480.

Tempesta D, Socci V, De Gennaro L, Ferrara M. 2018. Sleep and emotional processing. *Sleep Med Rev*. **40**:183–195.

van Driel J, Cox R, Cohen MX. 2015. Phase-clustering bias in phase–amplitude cross-frequency coupling and its removal. *J Neurosci Methods*. **254**:60–72.

Vaz AP, Inati SK, Brunel N, Zaghloul KA. 2019. Coupled ripple oscillations between the medial temporal lobe and neocortex retrieve human memory. *Science*. **363**:975–978.

Vijayan S, Lepage KQ, Kopell NJ, Cash SS. 2017. Frontal beta-theta network during REM sleep. *elife*. **6**:e18894.

Wagner T, Axmacher N, Lehnertz K, Elger CE, Fell J. 2010. Sleep-dependent directional coupling between human neocortex and hippocampus. *Cortex*. **46**:256–263.

Wagner U, Gais S, Born J. 2001. Emotional memory formation is enhanced across sleep intervals with high amounts of rapid eye movement sleep. *Learn Mem*. **8**:112–119.

Walker MP. 2009. The role of sleep in cognition and emotion. *Ann N Y Acad Sci*. **1156**:168–197.

Welch P. 1967. The use of fast Fourier transform for the estimation of power spectra: a method based on time averaging over short, modified periodograms. *IEEE Trans Audio Electroacoust*. **15**:70–73.

Wen H, Liu Z. 2016. Separating fractal and oscillatory components in the Power Spectrum of neurophysiological signal. *Brain Topogr*. **29**:13–26.

Wiesner CD, Pulst J, Krause F, Elsner M, Baving L, Pedersen A, Prehn-Kristensen A, Göder R. 2015. The effect of selective REM-sleep deprivation on the consolidation and affective evaluation of emotional memories. *Neurobiol Learn Mem*. **122**: 131–141.

Wilson M, McNaughton B. 1994. Reactivation of hippocampal ensemble memories during sleep. *Science*. **265**:676–679.

Zhang H, Fell J, Axmacher N. 2018. Electrophysiological mechanisms of human memory consolidation. *Nat Commun*. **9**:4103.

Zhang Y, Brady M, Smith S. 2001. Segmentation of brain MR images through a hidden Markov random field model and the expectation-maximization algorithm. *IEEE Trans Med Imaging*. **20**:45–57.